
Stabilization of 3D/2D perovskite heterostructures via inhibition of ion diffusion by cross-linked polymers for solar cells with improved performance

In the format provided by the authors and unedited

Table of contents

Supplementary Note 1-4

Supplementary Figure 1-22

Supplementary Table 1-6

Supplementary references

Supplementary Note 1: As shown in **Fig. 1c**, the pristine PbBr_2 film showed a characteristic diffraction peak at 18.48° , corresponding to the lattice plane of (020). After dipping the film in the FAI solution, this peak completely disappeared, and a new peak at 13.84° corresponding to the (001) plane of the 3D perovskite emerged. When PEG, PS and PMMA were coated onto the PbBr_2 film, the transition from PbBr_2 to 3D perovskite still proceeded, as evidenced by the emergence of (001) peaks with comparable intensities to those of the pristine PbBr_2 film. Notably, when the CLP was deposited on the PbBr_2 , the film maintained the (020) peak of PbBr_2 after dipping in the FAI solution, and the (001) peak corresponding to 3D perovskite was significantly weaker. The peak intensity and integral area are presented in **Supplementary Table 2**. When PbBr_2 films were dipped in the 4F-PEAI solution, similar results were observed. Pristine PbBr_2 reacted with 4F-PEAI, and formed $4\text{F-PEA}_2\text{Pb}(\text{I}_x\text{Br}_{1-x})_4$, showing a characteristic diffraction peak at 5.48° . When PEG, PS, and PMMA were used to cover the PbBr_2 film, the transition from PbBr_2 to 2D perovskite was not prevented. However, for PbBr_2 films covered with the CLP, the intensity of the (100) peak of 2D perovskite $4\text{F-PEA}_2\text{Pb}(\text{I}_x\text{Br}_{1-x})_4$ was significantly reduced. The peak intensity and integral area are presented in **Supplementary Table 3**. These results revealed that the CLP layer can effectively inhibit the intercalation of FA^+ and 4F-PEA^+ into the inorganic template of PbBr_2 .

Supplementary Note 2: pEDMA and the CLP were employed to prevent the reaction between PbBr_2 films and FAI at an elevated temperature of 100°C (**Supplementary Fig. 6**). The FAI solution was spin-coated on $\text{PbBr}_2/\text{pEDMA}$ and PbBr_2/CLP films, and annealed at 100°C for 10 to 300 min. After only 30 min, XRD patterns of $\text{PbBr}_2/\text{pEDMA}/\text{FAI}$ films showed a distinct peak corresponding to 3D perovskite. On the contrary, the diffraction peak of 3D perovskite in $\text{PbBr}_2/\text{CLP}/\text{FAI}$ films remained at a much weaker intensity even after 300 min of thermal annealing. This indicates that the CLP is more effective at inhibiting ion diffusion than pEDMA under thermal stress.

To investigate the stabilization effects of EDMA monomers and pEDMA in the 3D/2D perovskite heterostructures, we aged 3D/EDMA/2D and 3D/pEDMA/2D films at 100°C for 120 min, and compared the evolution of PL spectra. As shown in **Fig. 2d**, EDMA and pEDMA only offer partial stabilization the 3D/2D perovskite heterostructures under thermal stress. After thermal ageing, the PL emission intensity of 2D perovskite $4\text{F-PEA}_2\text{PbI}_4$ in both the 3D/EDMA/2D and 3D/pEDMA/2D films reduced, and PL emission of the quasi-2D perovskite $4\text{F-PEA}_2\text{FAPb}_2\text{I}_7$

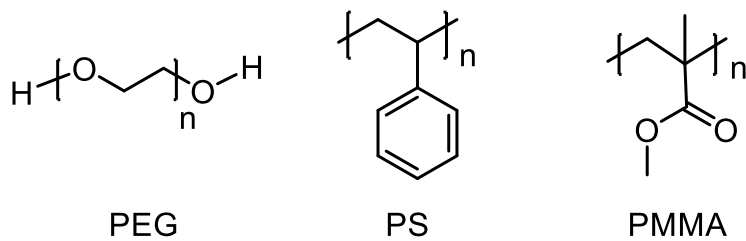
emerged. Thus, we conclude that the high degree of crosslinking and the network structure of the POSS-EDMA-based CLP play crucial roles in stabilizing the 3D/2D perovskite heterostructures.

Supplementary Note 3: It is challenging to directly measure the thickness of the CLP layer that was prepared using a concentration of 3 mg mL⁻¹. Instead, we prepared CLP layers with concentrations of 10, 15 and 20 mg mL⁻¹, and directly measured the thickness of the CLP layers using a profilometer (Bruker, Dektak). As shown in **Supplementary Figure 8a**, as the concentration increases from 10 to 20 mg mL⁻¹, the thickness of the as-prepared CLP layer increases from ~14 nm to ~40 nm. Using polynomial fitting to simulate the layer thicknesses, we estimate the thickness of the CLP layer for the concentration of 3 mg mL⁻¹ to be 2~3 nm. Additionally, we conducted XPS depth profiling, as shown in **Supplementary Figure 8b**. We used the signals of oxygen (O 1s) to track the existence of the CLP. After etching for only 30 seconds, the signals of oxygen disappeared. The etching rate of the argon gun towards the reference material (NPB, the molecular structure is shown in **Supplementary Figure 8c**) was calibrated to be 0.5~0.6 Å s⁻¹, and thus the thickness of the CLP layer should be below 1.8 nm.

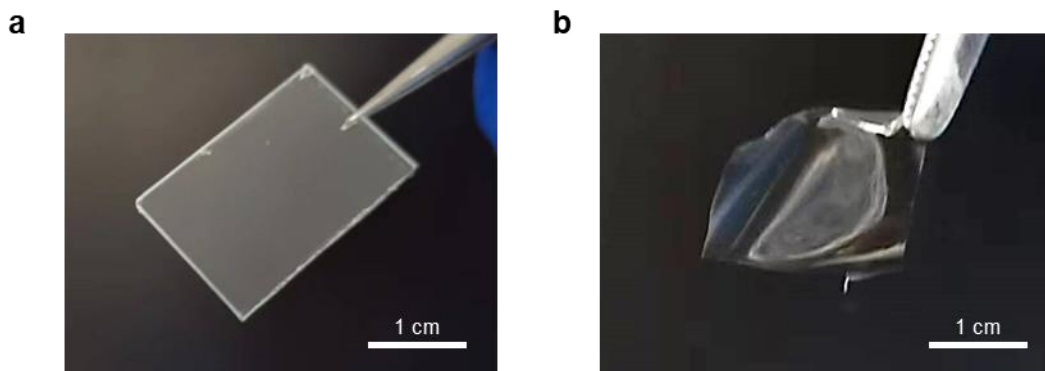
Supplementary Note 4: Previously, we have incorporated 3F-PEAI for surface treatment of 3D perovskite in *p-i-n* inverted PSCs^[5]. Herein, for *n-i-p* PSCs, the principle for selecting the organic ligand and tuning band alignment is entirely different. In *p-i-n* PSCs, the 2D layer on the surface of the 3D perovskite should be suitable for electron transfer and can block holes. However, this requirement is not easily met by regular 2D perovskite modification strategies. The 2D perovskite layer usually has a conduction band minimum (CBM) that is much higher than that of the 3D perovskite, which results in an electron-blocking effect. Thus, using a 2D perovskite layer on 3D perovskite in a *p-i-n* device is likely to reduce the efficiency of PSCs.

Using ultraviolet photoelectron spectroscopy (UPS) and absorption spectroscopy, the band alignment of low dimensional perovskite films of differing quantum well widths ($n = 1 - 4$) was estimated. It was found that quantum confinement upshifted the CBM, which induced electron blocking in *p-i-n* PSCs. In order to achieve efficient electron transfer, it is necessary to increase the n values of the low dimensional perovskites in order to minimize CBM offset. Using transient absorption (TA) spectra to evaluate the n values of the low-dimensional perovskites, it was revealed that the ligand of 3F-PEA produced low-dimensional perovskite containing majority $n =$

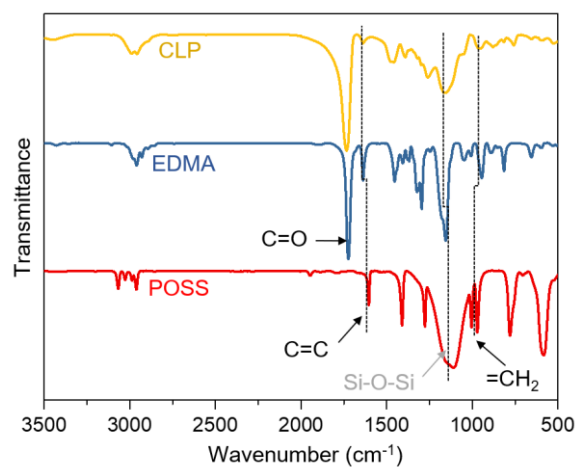
3, while 2F-PEA and 4F-PEA produced low dimensional perovskite containing majority $n = 2$. Therefore, we selected 3F-PEA as the target ligand to conduct further optimization in $p-i-n$ inverted PSCs. Herein, for $n-i-p$ PSCs in this work, the band alignment requirements for the 2D perovskite layer are the opposite. In $n-i-p$ devices, the 2D perovskite should have a CBM that is as high as possible to block electrons. Thus, we selected the ligand of 4F-PEA which produces the smallest n values when preparing low dimensional perovskites.



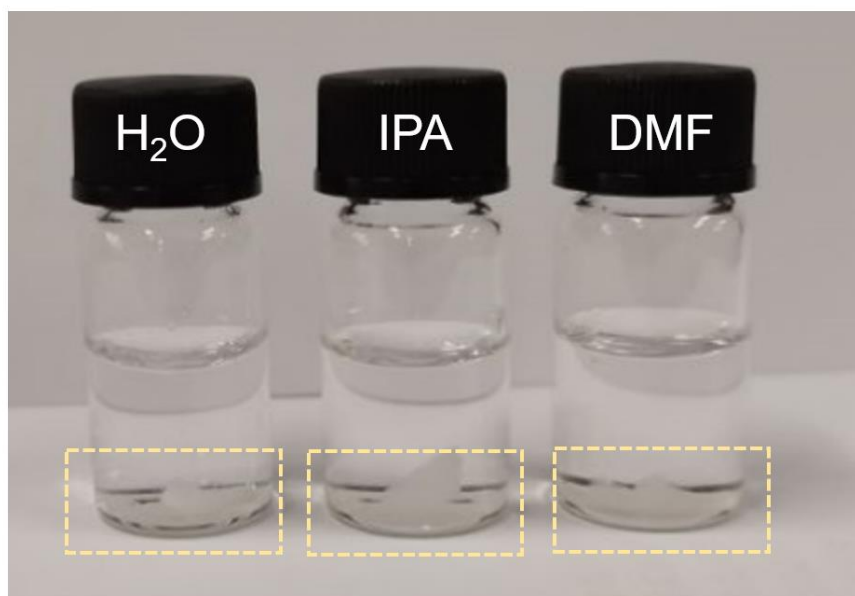
Supplementary Figure 1 | Molecular structures of polyethylene glycol (PEG), polystyrene (PS) and polymethyl methacrylate (PMMA).



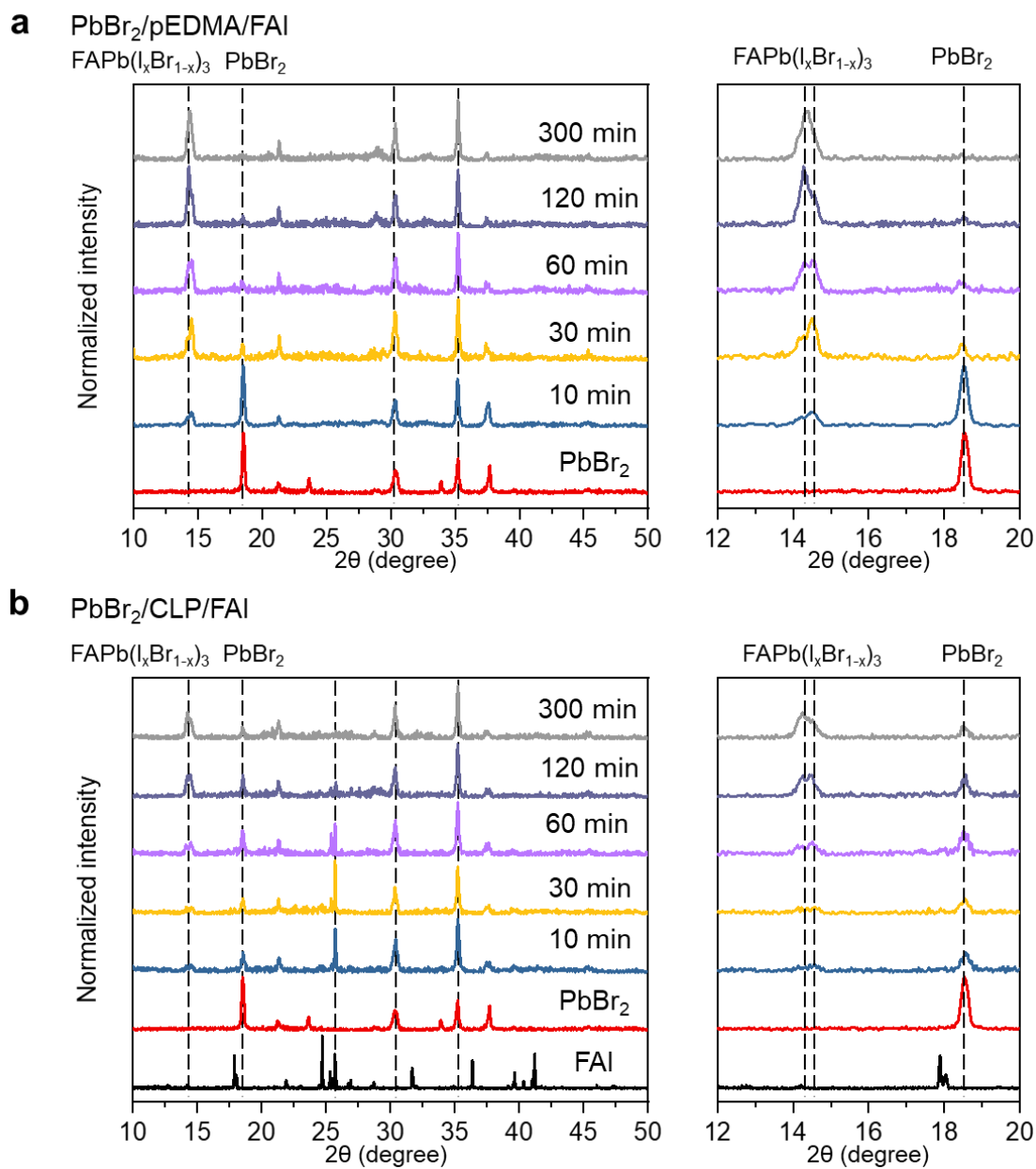
Supplementary Figure 2 | Photo of a CLP film on a glass substrate. a, The CLP thin film was deposited on the glass substrate by spin coating the CLP precursor solution (30 mg mL^{-1} in tetrahydrofuran) at 200 rpm for 30 seconds. **b,** The CLP thin film was separated from the glass substrate by a tweezer.



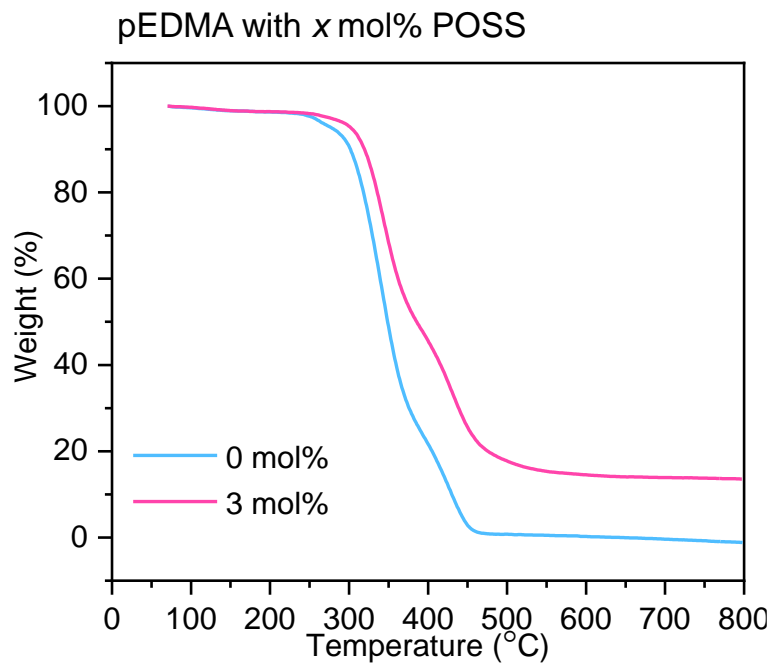
Supplementary Figure 3 | FTIR spectra of POSS, EDMA and CLP. Strong stretching vibration peaks of C=C and =CH₂ at 1640 cm⁻¹ and 903 cm⁻¹ are observed for EDMA and POSS, which reduce in intensity after annealing to form the CLP.



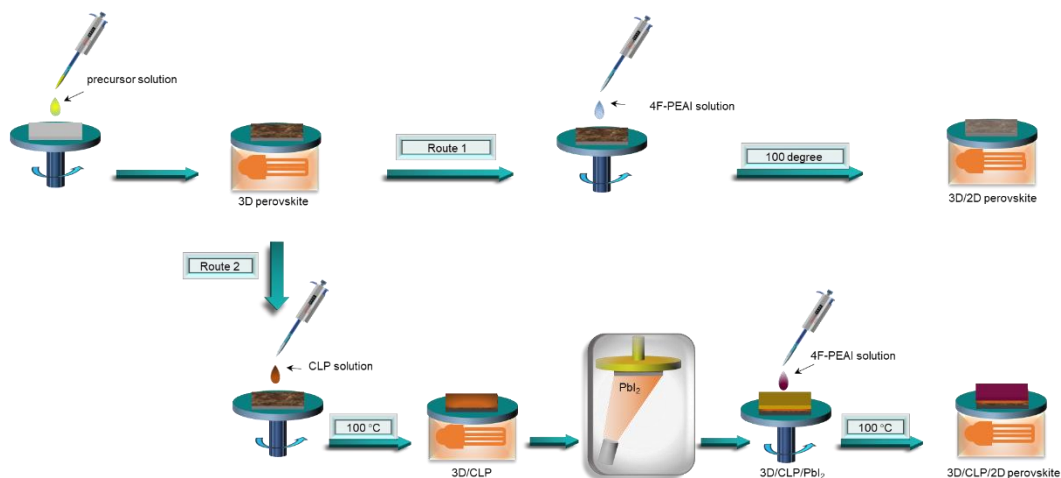
Supplementary Figure 4 | CLP submerged in common polar solvents of H₂O, IPA and dimethyl formamide (DMF).



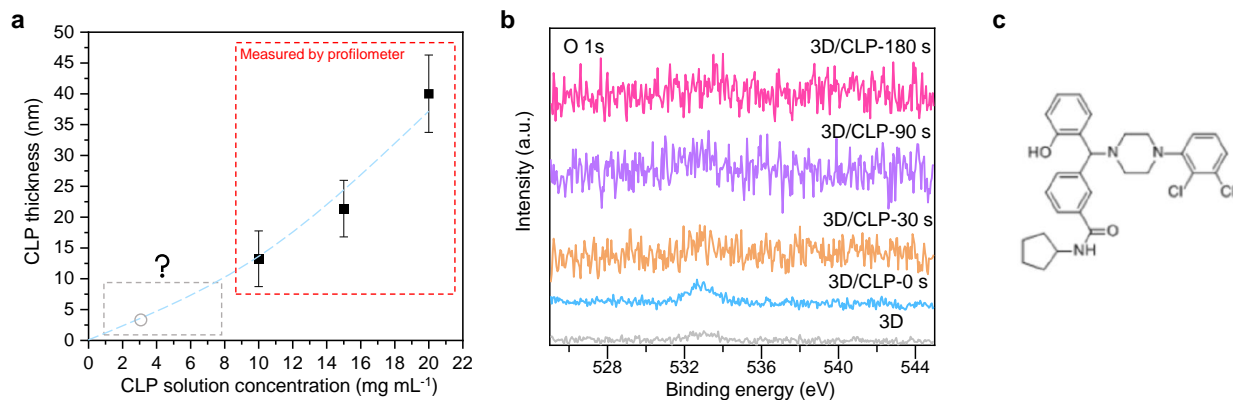
Supplementary Figure 5 | The XRD patterns of $\text{PbBr}_2/\text{pEDMA}/\text{FAI}$ (a) and $\text{PbBr}_2/\text{CLP}/\text{FAI}$ (b) under thermal stress at 100°C .



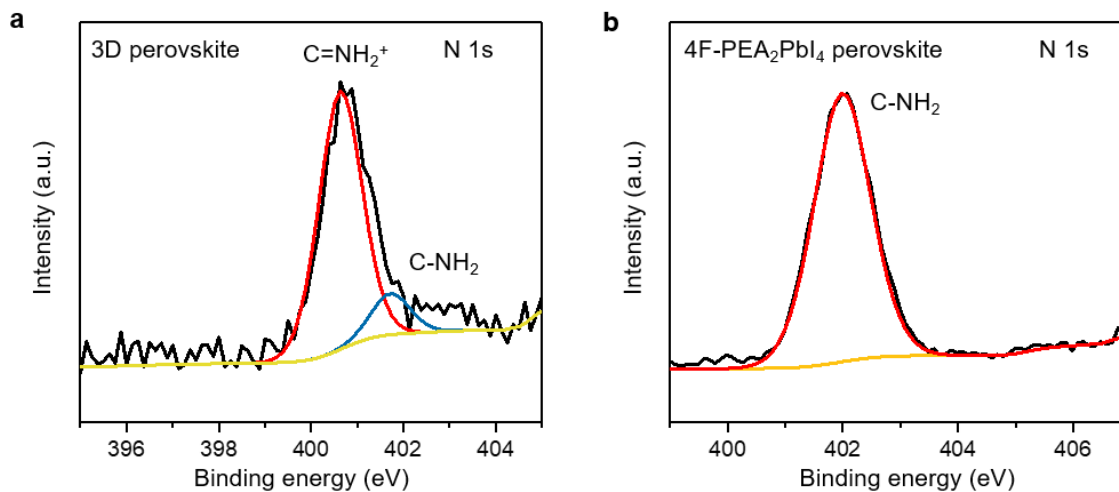
Supplementary Figure 6 | TGA of polymerized EDMA (pEDMA) with x mol% POSS.



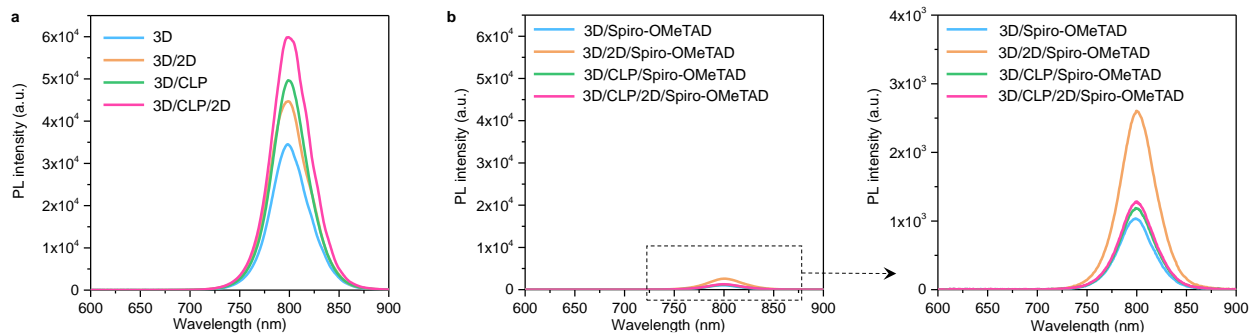
Supplementary Figure 7 | Fabrication routes of perovskite heterostructures. Route 1 is the traditional preparation process of a 3D/2D perovskite heterostructure by directly spin-coating a 4F-PEAI/IPA solution on the 3D perovskite surface. Route 2 is the preparation process of a 3D/CLP/2D perovskite heterostructure where the 2D perovskite is prepared by a vapor-assisted two-step process. CLP solution was prepared with 3 mg EDMA, POSS (3 mol% of EDMA) and 2,2'-Azobis(2-methylpropionitrile) initiator (2 wt% of EDMA) in 1ml of chlorobenzene and ethyl acetate mixed solution (v:v = 1:1).



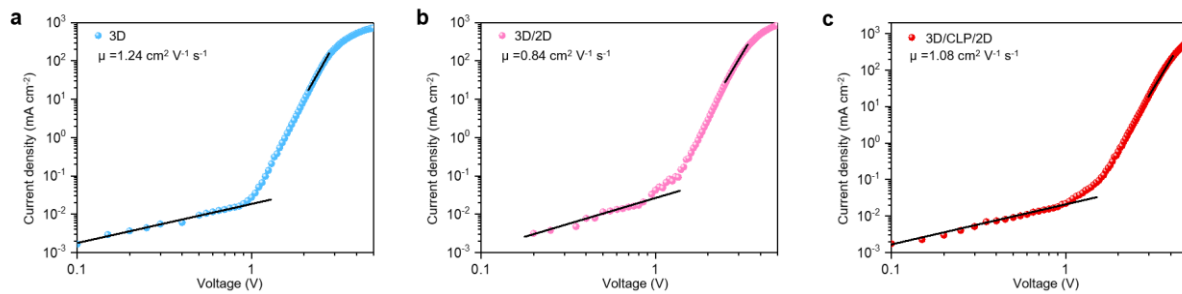
Supplementary Figure 8 | Estimation of the thickness of the CLP layer. **a**, The dependence of CLP layer thickness on solution concentration. The thicknesses of CLP layers prepared with the concentrations of 10, 15 and 20 mg mL⁻¹ are directly measured using a profilometer. Each average (symbol) and standard deviation (error bar) was calculated from the thickness values measured at 3 positions. The thickness of the CLP layer prepared with a concentration of 3 mg mL⁻¹ was estimated by fitting the results with a polynomial function. **b**, XPS in-depth profiling of 3D/CLP films. The signal for oxygen (O 1s) was used to track the CLP layer. **c**, Molecular structure of NPB, which was used as the reference for the Argon gun etching process.



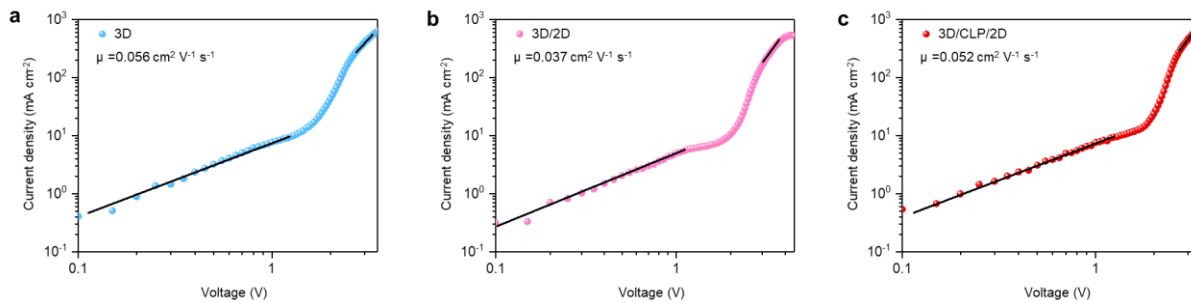
Supplementary Figure 9 | XPS spectra of 3D perovskite (FAPbI₃)_{0.95}(MAPbBr₃)_{0.05} (a) and 2D perovskite 4F-PEA₂PbI₄ (b). The peaks are fitted with Gaussian function.



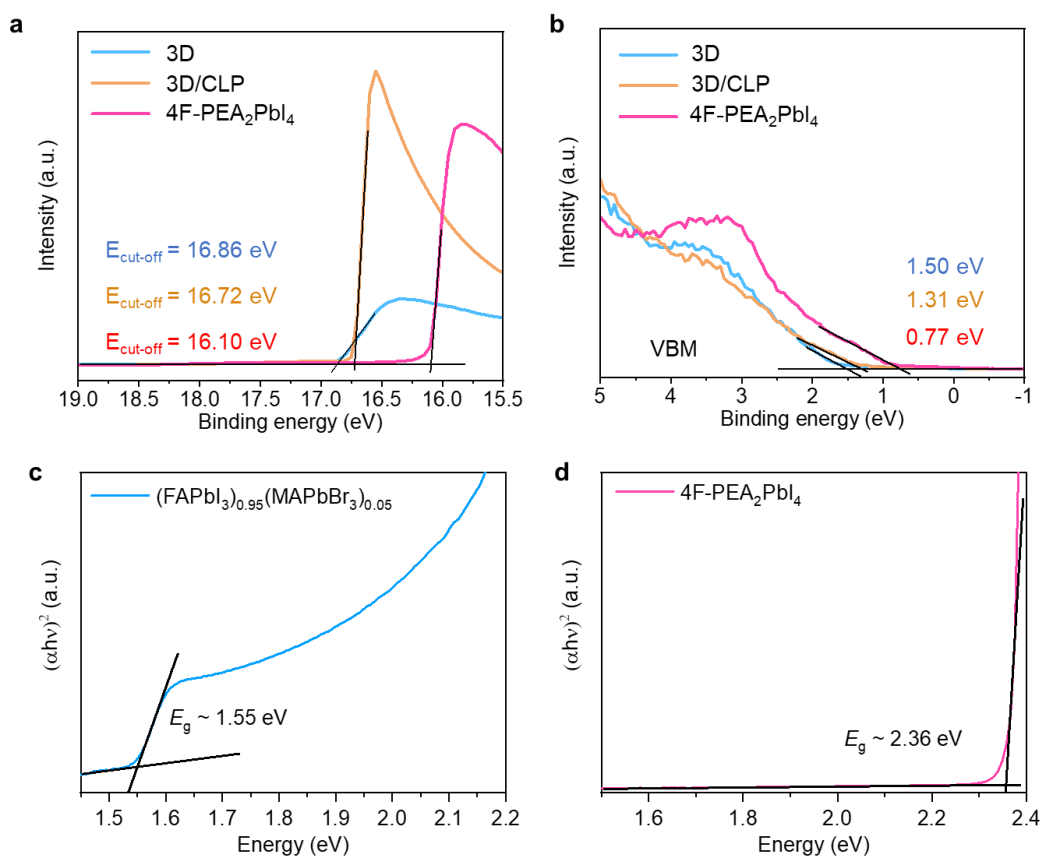
Supplementary Figure 10 | (a) The steady-state PL spectra of 3D perovskite, 3D/2D, 3D/CLP and 3D/CLP/2D heterostructures on glass substrates. (b) The steady-state PL spectra of 3D/Spiro-OMeTAD, 3D/2D/Spiro-OMeTAD, 3D/CLP/Spiro-OMeTAD and 3D/CLP/2D/Spiro-OMeTAD.



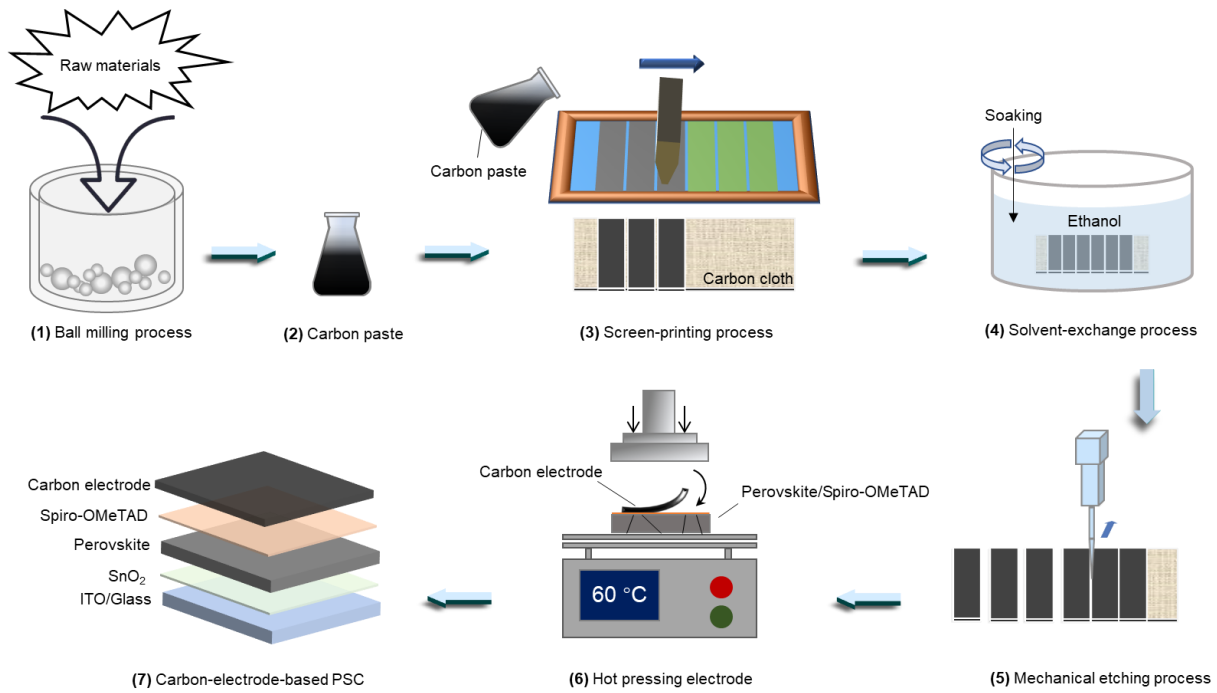
Supplementary Figure 11 | Dark J - V characteristics of electron-only devices (ITO/SnO₂/perovskite heterostructure/PCBM/Au) for 3D perovskite (a), 3D/2D (b) and 3D/CLP/2D (c) perovskite heterostructures. The specific segments of the curves are fitted with linear function.



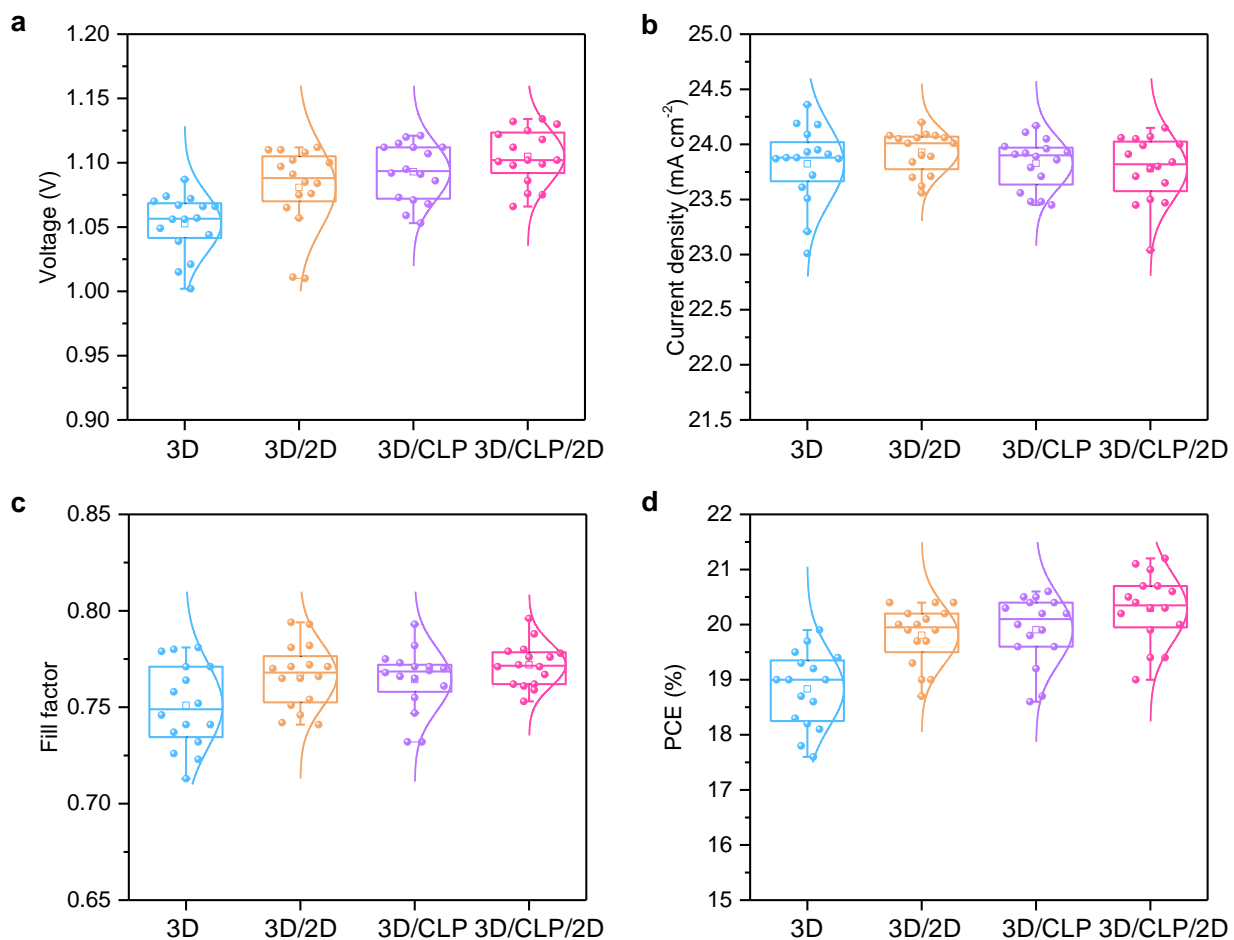
Supplementary Figure 12 | Dark J - V characteristics of hole-only devices (ITO/PTAA/perovskite heterostructure/Spiro-OMeTAD/Au) for 3D perovskite (a), 3D/2D (b) and 3D/CLP/2D (c) perovskite heterostructures. The specific segments of the curves are fitted with linear function.



Supplementary Figure 13 | Energy level analysis of 3D/CLP/2D perovskite heterostructures. **(a, b)** UPS spectra corresponding to the secondary electron onset region and the valence band maximums (VBMs) of 3D ((FAPbI₃)_{0.95}(MAPbBr₃)_{0.05}), 3D/CLP, and 2D (4F-PEA₂PbI₄) perovskite films. **(c, d)** Tauc plot of (FAPbI₃)_{0.95}(MAPbBr₃)_{0.05} and 4F-PEA₂PbI₄ showing determination of optical band gap from the intercept.

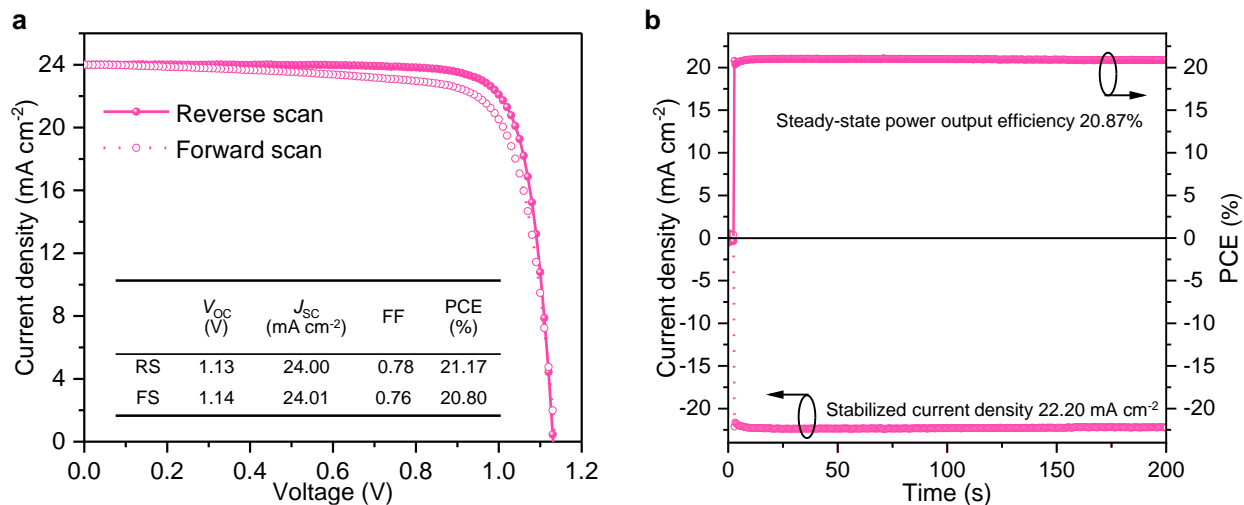


Supplementary Figure 14 | Preparation process of the carbon electrode based on screen-printing technique.

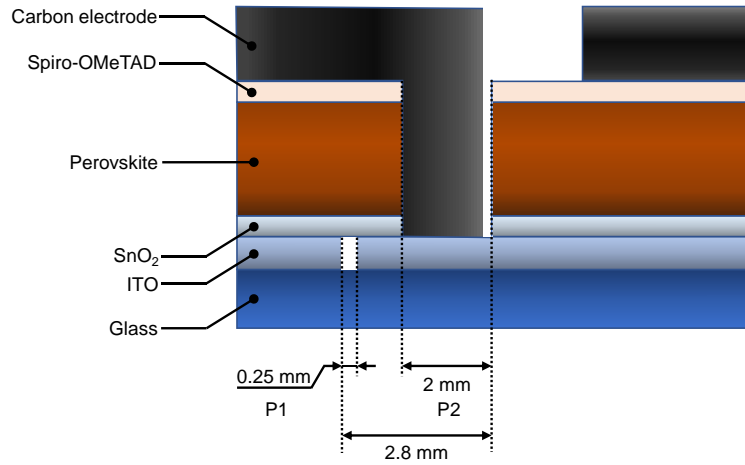


Supplementary Figure 15 | The statistics of photovoltaic performance parameters.

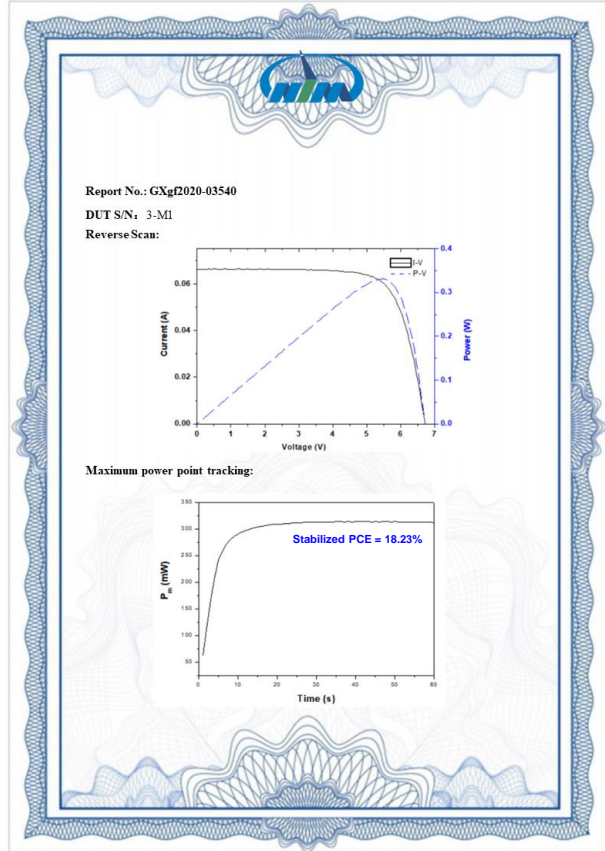
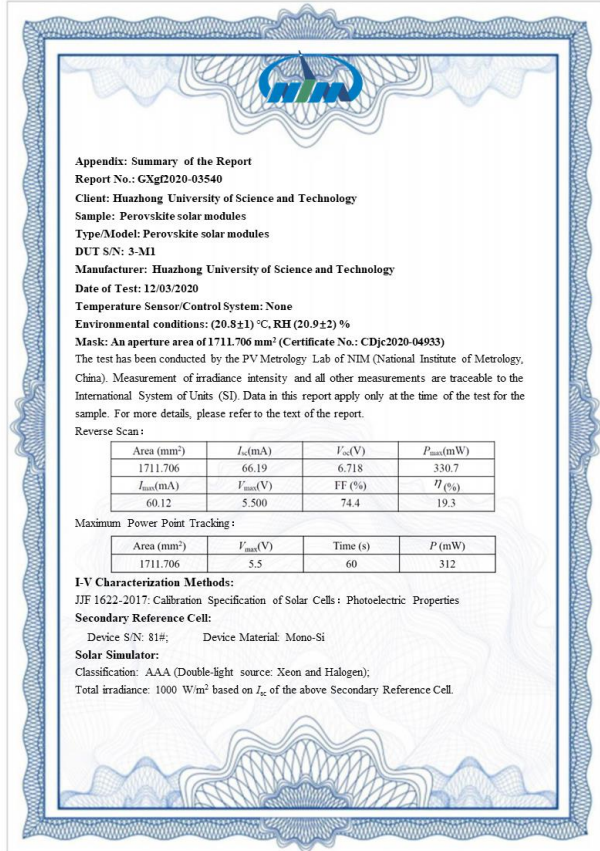
Comparison of the device performance obtained by 3D, 3D/2D, 3D/CLP and 3D/CLP/2D perovskite heterostructures. The standard error is represented in boxplots, for which the box extends from the 25th to the 75th percentiles, the empty squared dot depicts the average value, the short dash lines depict the minima and maxima. For each structure, sixteen cells were fabricated at the same condition.



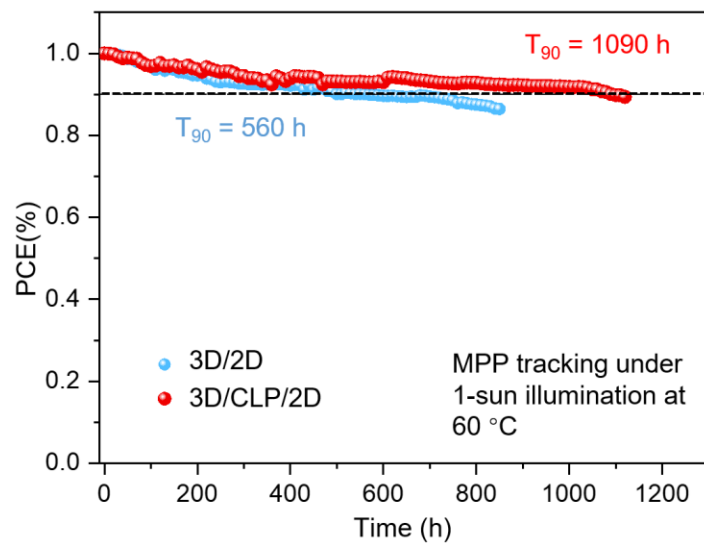
Supplementary Figure 16 | Device performance of 3D/CLP/2D PSCs. *J-V* curves measured at reverse and forward scan (a) and the stabilized output and calculated PCE of the device at a fixed bias (b).



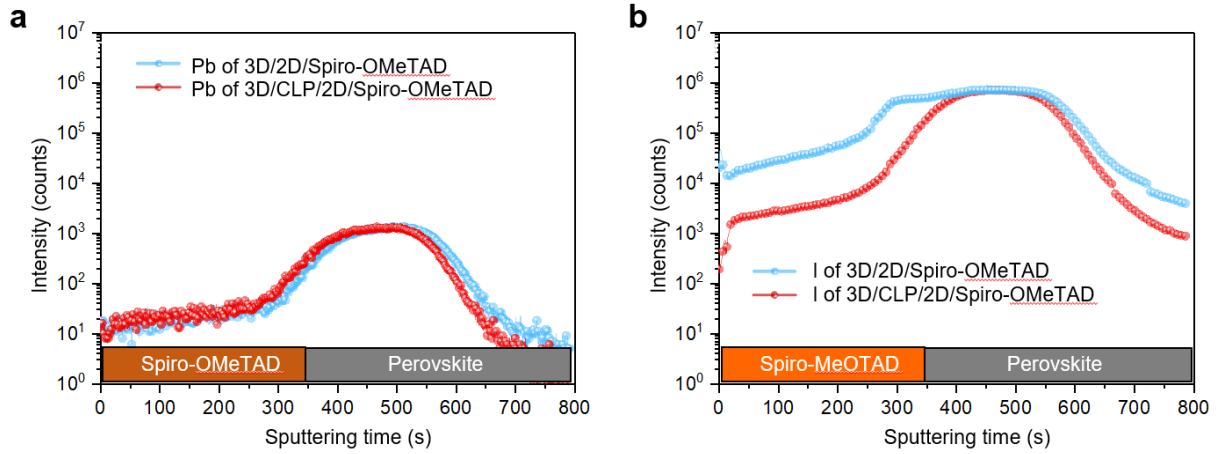
Supplementary Figure 17 | Schematic diagram of the cross-section of the perovskite solar module.



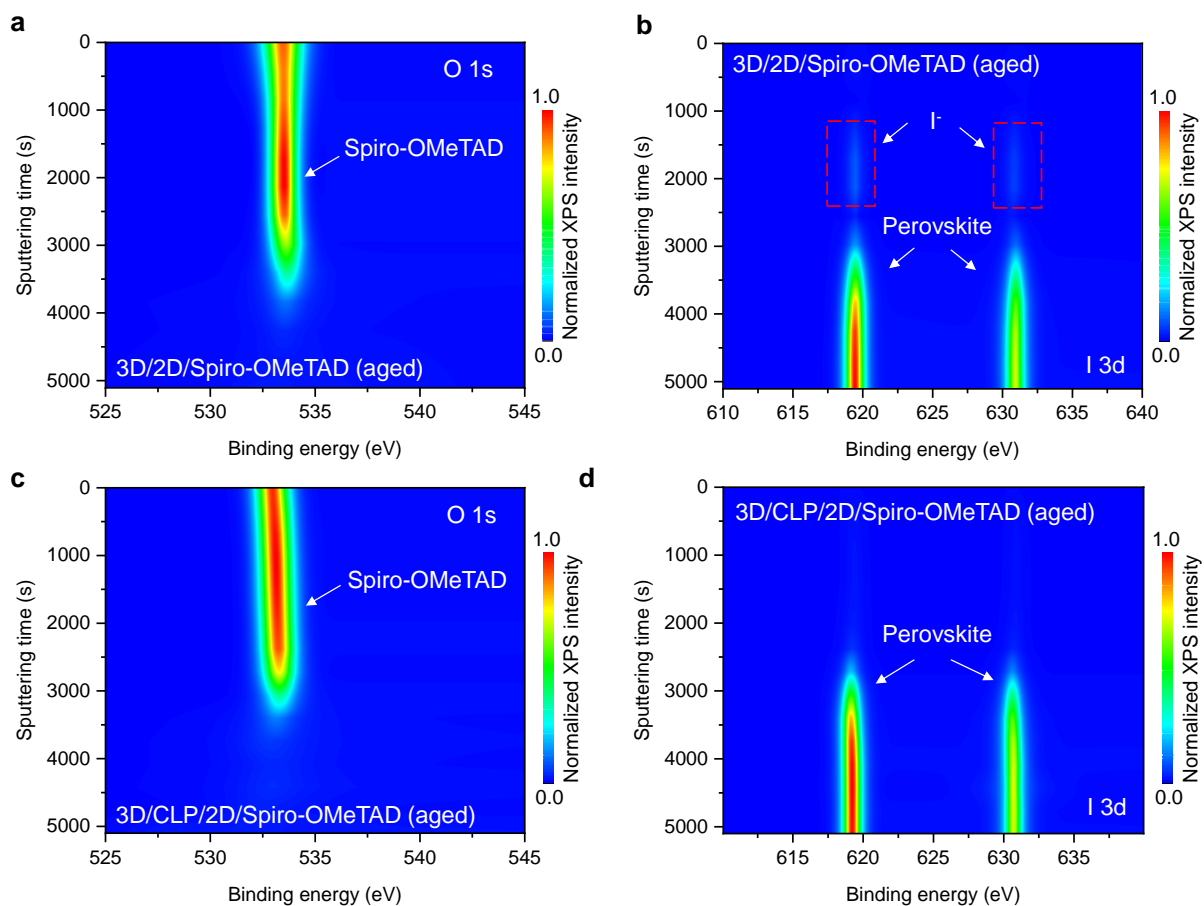
Supplementary Figure 18 | Certification of a PSM based on the 3D/CLP/2D perovskite heterostructure and carbon electrode. The aperture area is 17.1 cm², and the stabilized PCE is 18.23%. Certification is carried out by the National Institute of Metrology in China.



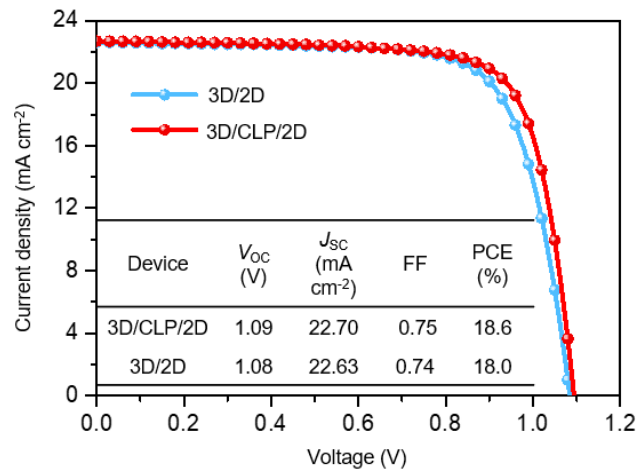
Supplementary Figure 19 | The operational stability of PSCs (SnO₂/perovskite heterostructure/Spiro-OMeTAD/Carbon) under continuous illumination in N₂ at ~60 °C. For the 3D/2D device, the initial efficiency was 20.2%. For the 3D/CLP/2D device, the initial efficiency was 21.0%.



Supplementary Figure 20 | TOF-SIMS of Pb (a) and I (b) ions in Spiro-OMeTAD and the perovskite layer.



Supplementary Figure 21 | Analysis of the iodide diffusion in 3D/2D/Spiro-OMeTAD and 3D/CLP/2D/Spiro-OMeTAD stacked layer. XPS depth profiling of oxygen (O 1s) of 3D/2D/Spiro-OMeTAD (a) and 3D/CLP/2D/Spiro-OMeTAD (c). The detection of oxygen corresponds to the Spiro-OMeTAD layer. XPS depth profiling of iodide (I 3d) of 3D/2D/Spiro-OMeTAD (b) and 3D/CLP/2D/Spiro-OMeTAD (d). The detection of iodide corresponds to the perovskite layer, and iodide that diffuses from the perovskite layer to the Spiro-OMeTAD layer.



Supplementary Figure 22 | Device performance obtained with P3HT-Spiro-OMeTAD. The J - V curves of PSCs with the structure of SnO₂/ (3D/2D perovskite)/P3HT-Spiro-OMeTAD/Carbon, and SnO₂/ (3D/CLP/2D perovskite)/P3HT-Spiro-OMeTAD/Carbon.

Supplementary Table 1 | Summary of reported operating stability of PSCs. The perovskite layer is treated with bulky organics, and the back contact is either metal (Au, Ag and Cu) or carbon. (Ref¹⁻¹⁹).

Perovskite passivation	Electrode	PCE/% (Aperture area/cm ²)	Lifetime (MPP)	T (°C)	Journal/Year
CLP/4F-PEAI	Carbon	21.17 (0.16)	T ₉₀ = 4392 hrs	60 °C	This work
CLP/4F-PEAI	Carbon	18.2 (17.1)	-	-	This work
MeO-PEAI (ST)	Au	25.8 (0.096)	T ₉₀ = ~ 500 hrs	-	<i>Nature</i> (2021, Ref. 1)
FAHCOO (BT) /OAI (ST)	Au	25.6 (0.08)	T ₈₅ = 450 hrs	35	<i>Nature</i> (2021, Ref. 2)
DMePDAI ₂ (ST)	Au	24.7 (0.12)	T ₉₀ = 1000 hrs	~ 40	<i>Science</i> (2021, Ref. 3)
OLAI (ST)	Ag	24.3 (0.07)	T ₉₅ = 500 hrs	~ 40	<i>Science</i> (2022, Ref. 4)
3F-PEAI/MAI (ST)	Ag	23.3 (0.05)	1000 hrs - no degradation	RT	<i>Nat. Photon.</i> (2022, Ref. 5)
3F-PEAI/MAI (ST)	Ag	23.3 (0.05)	T ₉₂ = 500 hrs	65	<i>Nat. Photon.</i> (2022, Ref. 5)
choline chloride (ST)	Au	23.1 (0.16)	T ₉₀ = 500 hrs	RT	<i>Science</i> (2020, Ref. 6)
i-BABr (ST)	Au	20.42 (17.1)	T ₈₂ = 500 hrs	RT	<i>Science</i> (2021, Ref. 7)
BA ₂ PbI ₄ (ST)	Au	24.35 (0.094)	T ₉₈ = 1620 hrs	-	<i>Nat. Energy</i> (2021, Ref. 8)
EAI/MAI (ST)	Au	16.6 (22.4)	T ₉₀ = 1570 hrs	40	<i>Nat. Energy</i> (2020, Ref. 9)
OATsO (ST)	Au	24 (0.13)	800 hrs - no degradation	40	<i>Nature</i> (2022, Ref. 10)
iPAmHCl (BT)	Au	23.9 (0.16)	2000 hrs - no degradation	RT	<i>Nat. Energy</i> (2021, Ref. 11)
-	Au	24.04 (0.08)	T ₉₅ = ~ 2000 hrs	RT	<i>Science</i> (2021, Ref. 12)
-	rGO/ Au	20.4 (0.16)	T ₉₅ = 1000 hrs	60	<i>Science</i> (2019, Ref. 13)
-	Ag	22.02 (0.13)	T ₉₂ = 1000 hrs	85	<i>Nat. Nanotechnol.</i> (2020, Ref. 14)
PbPyA ₂ /TMS (ST)	Cu	24.3 (0.09)	T ₉₀ = 1000 hrs	55	<i>Science</i> (2022, Ref. 15)
lead sulfate (ST)	Cu	21.1 (-)	T ₉₇ = 1200 hrs	65	<i>Science</i> (2019, Ref. 16)
-	Cu	20.1 (17.9)	550 hrs - no degradation	60	<i>Science</i> (2021, Ref. 17)
-	Ti ₁ -rGO/FTO	20.6 (0.09)	T ₉₅ = 1300 hrs	60	<i>Nat. energy</i> (2021, Ref. 18)
-	Au/MgF ₂	20.9 (0.113)	1400 hrs - no degradation	60~65	<i>Nat. Energy</i> (2021, Ref. 19)

Note:

4-methoxy-phenethylammonium iodide: MeO-PEAI; octylammonium iodide: OAI; Octylammonium tosylate: OATsO; N, N-dimethyl-1,3-propane diammonium diiodide: DMePDAI₂; Oleylammonium iodide: OLAI; isobutylamine bromide: i-BABr. 3-iodopropyl trimethoxysilane [Si (OCH₃)₃(CH₂)₃I]: I-SAM; Polyethylenimine: PEIE; poly[2,2''''-bis[[2-butylloctyl]oxy]carbonyl [2,2':5',2'':5'',2''''-quaterthiophene]-5,5''''-diyl]: PDCBT; BCF-doped poly(triarylamine): PTAA-BCF; 4-fluoro-phenethylammonium iodide: 4F-PEAI; 3-fluoro-phenethylammonium: 3F-PEAI; pyrene-based ethylammonium iodide: PREAI; isopropylammonium chloride: iPAmHCl; n-hexyl trimethyl ammonium bromide: HTABr; ethylenediaminetetraacetic acid dipotassium salt: EDTAK; ethylammonium iodide: EAI; aminovaleric acid iodide: AVAI; 5-ammoniumvaleric acid iodide: 5-AVAI; 1-butyl-3-methylimidazolium tetrafluoroborate: BMIMBF₄; Pyridine-2-carboxylic lead: PbPyA₂; Hexamethyldisilathiane: TMS; Maximum power point tracking: MPPT; Surface treatment: ST; Bulk treatment: BT; Room temperature: RT.

Supplementary Table 2 | Peak intensity and integral area obtained from the (001) peak of 3D perovskite and the (020) peak of PbBr₂ for different samples.

Samples	Peak intensity/ (001) _{3D}	Peak area/ (001) _{3D}	Peak intensity/ (020) _{PbBr₂}	Peak area/ (020) _{PbBr₂}
PbBr ₂ /CLP + FAI	2980	860.9	4720	1284.1
PbBr ₂ /pEDMA + FAI	3160	1957.2	5750	2027.8
PbBr ₂ /PMMA + FAI	12780	3340.5	-	-
PbBr ₂ /PS + FAI	12540	3396.1	-	-
PbBr ₂ /PEG + FAI	13140	2900.3	-	-
PbBr ₂ /EDMA + FAI	16761	4631.1	-	-
Pristine PbBr ₂ + FAI	17360	3683.9	-	-
PbBr ₂	-	-	7940	1858

Supplementary Table 3 | Peak intensity and integral area obtained from the (100) peak of 2D perovskite and (020) peak of PbBr₂ for different samples.

Samples	Peak intensity/ (100) _{2D}	Peak area/ (100) _{2D}	Peak intensity/ (020) _{PbBr₂}	Peak area/ (020) _{PbBr₂}
PbBr ₂ /CLP + 4F-PEAI	12130	1701.2	5190	1246.5
PbBr ₂ /pEDMA + 4F-PEAI	13132	2995.94	5334	1414.3
PbBr ₂ /PMMA + 4F-PEAI	69936	10773.73	-	-
PbBr ₂ /PS + 4F-PEAI	45850	8193.18	-	-
PbBr ₂ /PEG + 4F-PEAI	37900	6635.57	-	-
PbBr ₂ /EDMA + 4F-PEAI	111407	22590.81	-	-
Pristine PbBr ₂ + 4F-PEAI	156555	26662.17	-	-
PbBr ₂	-	-	10600	2635.4

Supplementary Table 4 | The fitted parameters from TRPL of various perovskite samples.

Samples	A ₁	τ ₁	A ₂	τ ₂	τ _{avg} (ns)
Pristine 3D	0.569	91	0.431	455	248
3D/2D	0.527	84	0.473	574	315
3D/CLP	0.562	134	0.438	607	341
3D/CLP/2D	0.491	89	0.509	825	424
Pristine 3D/ Spiro-OMeTAD	0.645	5.6	0.355	55	23
3D/2D/Spiro- OMeTAD	0.639	7.7	0.361	68	30
3D/CLP/ Spiro- OMeTAD	0.643	6.1	0.357	59	25
3D/CLP/2D /Spiro-OMeTAD	0.641	6.7	0.359	62	27

Note: The measured PL decay kinetics are fitted by bi-exponential decay function as follow

$$F(t) = A_1 \exp(-t/\tau_1) + A_2 \exp(-t/\tau_2)$$

$$\text{The average lifetime: } \tau_{avg} = (A_1 * \tau_1 + A_2 * \tau_2)/(A_1 + A_2)$$

Supplementary Table 5 | The photovoltaic parameters of PSCs fabricated with 3D, 3D/2D, 3D/CLP, and 3D/CLP/2D perovskite heterostructures.

Active layer	V_{oc} (V)	J_{sc} (mA cm⁻²)	FF	PCE (%)
3D	1.05 ± 0.02	23.82 ± 0.35	0.75 ± 0.02	18.83 ± 0.69
3D/2D	1.08 ± 0.03	23.93 ± 0.19	0.76 ± 0.02	19.81 ± 0.54
3D/CLP	1.09 ± 0.02	23.83 ± 0.23	0.76 ± 0.02	19.91 ± 0.63
3D/CLP/2D	1.10 ± 0.02	23.78 ± 0.30	0.77 ± 0.01	20.29 ± 0.63

Supplementary Table 6 | Summary of reported performance for state-of-the-art PSCs using carbon electrodes. (Ref^{18,20-35})

Device structure	Area/ cm ²	V _{oc} (V)	J _{sc} (mA cm ⁻²)	FF	PCE (%)	Journal/ Year
ITO/SnO ₂ /Perovskite/CLP/2D/Spiro-OMeTAD/Carbon	0.16	1.13	24	0.78	21.2	This work
ITO/SnO ₂ /Perovskite/CLP/2D/Spiro-OMeTAD/Carbon	17.1	6.73	3.87	0.75	19.6	This work
FTO/c-TiO ₂ /(m-TiO ₂ /m-ZrO ₂ /m-C)/Perovskite	0.07	0.858	22.8	0.66	12.8	<i>Science</i> (2014, Ref. 20)
FTO/c-TiO ₂ /(m-TiO ₂ /m-ZrO ₂ /m-C)/Perovskite	0.8	0.94	23.8	0.66	14.89	<i>Joule</i> (2020, Ref. 21)
FTO/m-TiO ₂ /Perovskite/CuPc/Carbon	0.09	1.05	20.8	0.74	16.1	<i>Nano Energy</i> (2016, Ref. 22)
FTO/c-TiO ₂ /(m-TiO ₂ /m-ZrO ₂ /m-C)/Perovskite	0.108	1.023	22.25	0.767	17.47	<i>Adv. Energy Mater.</i> (2021, Ref. 23)
ITO/SnO ₂ /perovskite/spiro-OMeTAD/TFMS-CNT	0.1	1.01	24.21	0.72	17.5	<i>Nano Lett.</i> (2019, Ref. 24)
FTO/c-TiO ₂ /(m-TiO ₂ /m-ZrO ₂ /m-C)/Perovskite	0.1018	0.956	24.26	0.762	17.68	<i>Adv. Energy Mater.</i> (2022, Ref. 25)
ITO/PTAA/Perovskite/C ₆₀ /SnO ₂ /Carbon	0.06	1.04	22.6	0.769	18.1	<i>Nat. Energy</i> (2020, Ref. 26)
FTO/c-TiO ₂ /m-TiO ₂ /Perovskite/2D/Carbon	0.1	1.03	24.3	0.739	18.5	<i>Adv. Energy Mater.</i> (2022, Ref. 27)
ITO/APTES/C ₆₀ /Perovskite/Carbon	0.08	1.12	22.72	0.73	18.64	<i>Angew. Chem. Int. Ed.</i> (2021, Ref. 28)
FTO/SnO ₂ /Perovskite/Spiro-OMeTAD/Graphene/FTO	0.09	1.05	22.78	0.78	18.65	<i>Energy Environ. Sci.</i> (2019, Ref. 29)
FTO/c-TiO ₂ /m-TiO ₂ /Perovskite/Spiro-OMeTAD/Carbon	0.1	1.08	23.33	0.762	19.2	<i>Adv. Funct. Mater.</i> (2018, Ref. 30)
FTO/c-TiO ₂ /m-TiO ₂ /Perovskite/Spiro-OMeTAD/Ti-rGO/FTO	0.09	1.059	26.0	0.785	21.6	<i>Nat. Energy</i> (2021, Ref. 18)
FTO/SnO ₂ /perovskite/D-MWCNT:Spiro-OMeTAD/Graphene/FTO	0.049	1.08	25.9	0.78	22.07	<i>Adv. Funct. Mater.</i> (2022, Ref. 31)
FTO/c-TiO ₂ /(m-TiO ₂ /m-ZrO ₂ /m-C)/Perovskite	70	9.63	2.95	0.629	10.75	<i>Energy Environ. Sci.</i> (2016, Ref. 32)
FTO/c-TiO ₂ /(m-TiO ₂ /m-ZrO ₂ /m-C)/Perovskite	50	7.05	2.247	0.704	11.2	<i>Nat. Commun.</i> (2017, Ref. 33)
FTO/c-TiO ₂ /(m-TiO ₂ /m-ZrO ₂ /m-C)/Perovskite	60.87	8.50	2.50	0.61	12.87	<i>Nano Energy</i> (2020, Ref. 34)
ITO/SnO ₂ /Perovskite/PDCBT/Ta-WO _x /Carbon	4	4.2	5.3	0.69	15.3	<i>Adv. Energy Mater.</i> (2021, Ref. 35)

Note: Mesoscopic TiO₂: m-TiO₂; Mesoscopic ZrO₂: m-ZrO₂; Mesoscopic Carbon: m-C; Copper phthalocyanine: CuPc; Trifluoromethanesulfonic acid vapor doping of carbon nanotube: TFMS-CNT; single titanium (Ti) adatoms anchored on reduced graphene oxide: Ti-rGO; defective multi-walled carbon nanotube: D-MWCNT; poly[(4,4'-bis(2-butyltioxycarbonyl)-[2,2'-bithiophene]-5,5'-diyl)-alt-(2,2'-bithiophene-5,5'-diyl)]: PDCBT; Tantalum doped tungsten oxide: Ta-WO_x.

Supplementary References

1. Min, H. *et al.* Perovskite solar cells with atomically coherent interlayers on SnO₂ electrodes. *Nature* **598**, 444-450 (2021).
2. Jeong, J. *et al.* Pseudo-halide anion engineering for α -FAPbI₃ perovskite solar cells. *Nature* **592**, 381-385 (2021).
3. Zhang, F. *et al.* Metastable Dion-Jacobson 2D structure enables efficient and stable perovskite solar cells. *Science* **375**, 71-76 (2021).
4. Azmi, R. *et al.* Damp heat-stable perovskite solar cells with tailored-dimensionality 2D/3D heterojunctions. *Science* **376**, 73-77 (2022).
5. Chen, H. *et al.* Quantum-size-tuned heterostructures enable efficient and stable inverted perovskite solar cells. *Nat. Photon.* **16**, 352-358 (2022).
6. Lu, H. *et al.* Vapor-assisted deposition of highly efficient, stable black-phase FAPbI₃ perovskite solar cells. *Science* **370**, eabb8985 (2020).
7. Bu, T. *et al.* Lead halide-templated crystallization of methylamine-free perovskite for efficient photovoltaic modules. *Science* **372**, 1327-1332 (2021).
8. Jang, Y.-W. *et al.* Intact 2D/3D halide junction perovskite solar cells via solid-phase in-plane growth. *Nat. Energy* **6**, 63-71 (2021).
9. Liu, Z. *et al.* A holistic approach to interface stabilization for efficient perovskite solar modules with over 2,000-hour operational stability. *Nat. Energy* **5**, 596-604 (2020).
10. Tan, S. *et al.* Stability-limiting heterointerfaces of perovskite photovoltaics. *Nature* **605**, 268-273 (2022).
11. Park, B.-W. *et al.* Stabilization of formamidinium lead triiodide α -phase with isopropylammonium chloride for perovskite solar cells. *Nat. Energy* **6**, 419-428 (2021).
12. Li, N. *et al.* Liquid medium annealing for fabricating durable perovskite solar cells with improved reproducibility. *Science* **373**, 561-567 (2021).
13. Arora, N. *et al.* Perovskite solar cells with CuSCN hole extraction layers yield stabilized efficiencies greater than 20%. *Science* **358**, 768-771 (2017).
14. Wu, S. *et al.* 2D metal-organic framework for stable perovskite solar cells with minimized lead leakage. *Nat. Nanotechnol.* **15**, 934-940 (2020).
15. Li, X. *et al.* Constructing heterojunctions by surface sulfidation for efficient inverted perovskite solar cells. *Science* **375**, 434-437 (2022).
16. Yang, S. *et al.* Stabilizing halide perovskite surfaces for solar cell operation with wide-bandgap lead oxysalts. *Science* **365**, 473-478 (2019).
17. Chen, S. *et al.* Stabilizing perovskite-substrate interfaces for high-performance perovskite modules. *Science* **373**, 902-907 (2021).
18. Zhang, C. *et al.* Ti₁-graphene single-atom material for improved energy level alignment in perovskite solar cells. *Nat. Energy* **6**, 1154-1163 (2021).
19. Zhao, Y. *et al.* A bilayer conducting polymer structure for planar perovskite solar cells with over 1,400 hours operational stability at elevated temperatures. *Nat. Energy* **7**, 144-152 (2021).
20. Mei, A. *et al.* A hole-conductor-free, fully printable mesoscopic perovskite solar cell with high stability. *Science* **345**, 295-298 (2014).
21. Mei, A. *et al.* Stabilizing perovskite solar cells to IEC61215:2016 standards with over 9,000-h operational tracking. *Joule* **4**, 2646-2660 (2020).
22. Zhang, F. *et al.* Boosting the efficiency and the stability of low cost perovskite solar cells by using CuPc nanorods as hole transport material and carbon as counter electrode. *Nano Energy* **20**, 108-116 (2016).
23. Chen, X. *et al.* Tailoring the dimensionality of hybrid perovskites in mesoporous carbon electrodes for type-II band alignment and enhanced performance of printable hole-conductor-free perovskite solar cells. *Adv. Energy Mater.* **11**, 2100292 (2021).
24. Lee, J.-W. *et al.* Vapor-assisted ex-situ doping of carbon nanotube toward efficient and stable perovskite solar cells. *Nano Lett.* **19**, 2223-2230 (2019).
25. Du, J. *et al.* Minimizing the voltage loss in hole-conductor-free printable mesoscopic perovskite solar cells. *Adv. Energy Mater.* **12**, 2102229 (2022).
26. Chen, S. *et al.* Trapping lead in perovskite solar modules with abundant and low-cost cation-exchange resins. *Nat. Energy* **5**, 1003-1010 (2020).
27. Zouhair, S. *et al.* Employing 2D-perovskite as an electron blocking layer in highly efficient (18.5%) perovskite solar cells with printable low temperature carbon electrode. *Adv. Energy Mater.* **12**, 2200837 (2022).

28. Tian, T. *et al.* Interfacial linkage and carbon encapsulation enable full solution-printed perovskite photovoltaics with prolonged lifespan. *Angew. Chem. Int. Ed.* **60**, 23735-23742 (2021).
29. Zhang, C. *et al.* Efficient stable graphene-based perovskite solar cells with high flexibility in device assembling via modular architecture design. *Energy Environ. Sci.* **12**, 3585-3594 (2019).
30. Zhang, H. *et al.* Self-adhesive macroporous carbon electrodes for efficient and stable perovskite solar cells. *Adv. Funct. Mater.* **28**, 1802985 (2018).
31. Wang, Y. *et al.* Defective MWCNT enabled dual interface coupling for carbon-based perovskite solar cells with efficiency exceeding 22%. *Adv. Funct. Mater.* **32**, 2204831 (2022).
32. Priyadarshi, A. *et al.* A large area (70 cm²) monolithic perovskite solar module with a high efficiency and stability. *Energy Environ. Sci.* **9**, 3687-3692 (2016).
33. Grancini, G. *et al.* One-Year stable perovskite solar cells by 2D/3D interface engineering. *Nat. Commun.* **8**, 15684 (2017).
34. Xu, M. *et al.* Efficient triple-mesoscopic perovskite solar mini-modules fabricated with slot-die coating. *Nano Energy* **74**, 104842 (2020).
35. Yang, F. *et al.* Low temperature processed fully printed efficient planar structure carbon electrode perovskite solar cells and modules. *Adv. Energy Mater.* **11**, 2101219 (2021).